

Synthesis and electronic properties of epitaxial SrNiO<sub>3</sub>/SrTiO<sub>3</sub> superlattices

Le Wang<sup>1,\*</sup>, Jiali Zhao,<sup>2,3</sup> Cheng-Tai Kuo<sup>4</sup>, Bethany E. Matthews<sup>5</sup>, Marjolein T. Oostrom<sup>6</sup>, Steven R. Spurgeon<sup>5,7</sup>, Zhenzhong Yang,<sup>1</sup> Mark E. Bowden,<sup>8</sup> Linda W. Wangoh,<sup>1</sup> Sang-Jun Lee<sup>4</sup>, Jun-Sik Lee<sup>4</sup>, Er-Jia Guo<sup>3</sup>, Jiaou Wang,<sup>2</sup> Scott A. Chambers<sup>1</sup> and Yingge Du<sup>1,†</sup>

<sup>1</sup>Physical and Computational Sciences Directorate, Pacific Northwest National Laboratory, Richland, Washington 99354, USA

<sup>2</sup>Beijing Synchrotron Radiation Facility, Institute of High Energy Physics, Chinese Academy of Sciences, Beijing, 100039 China

<sup>3</sup>Beijing National Laboratory for Condensed Matter Physics and Institute of Physics, Chinese Academy of Sciences, Beijing 100190, China

<sup>4</sup>Stanford Synchrotron Radiation Lightsource, SLAC National Accelerator Laboratory, Menlo Park, California 94025, USA

<sup>5</sup>Energy and Environment Directorate, Pacific Northwest National Laboratory, Richland, Washington 99352, USA

<sup>6</sup>National Security Directorate, Pacific Northwest National Laboratory, Richland, Washington 99352, USA

<sup>7</sup>Department of Physics, University of Washington, Seattle, Washington 98195, USA

<sup>8</sup>Environmental Molecular Sciences Laboratory, Pacific Northwest National Laboratory, Richland, Washington 99352, USA



(Received 13 April 2022; accepted 27 June 2022; published 20 July 2022)

We report the deposition and characterization of a set of high-quality (SrNiO<sub>3</sub>)<sub>1</sub>/(SrTiO<sub>3</sub>)<sub>*n*</sub> superlattices using oxide molecular beam epitaxy. We demonstrate that one unit cell of SrNiO<sub>3</sub> can be stabilized as a perovskite in these structures and that there is no charge transfer across the heterointerface. Detailed spectroscopy data analysis indicates that holes are confined to the SrNiO<sub>3</sub> unit cells, resulting in a Ni valence between 3 and 4. Hole hopping conductivity is observed in the *n* = 1 superlattice but is strongly suppressed along the *c*-axis direction for *n* = 3 and 5, resulting in the insulating behavior in the latter. Our study will inspire the epitaxial synthesis of (SrNiO<sub>3</sub>)<sub>1</sub>/(RNiO<sub>3</sub>)<sub>*n*</sub> superlattices, as measurements of their properties could open a platform for studying nickelate-based superconductors.

DOI: [10.1103/PhysRevMaterials.6.075006](https://doi.org/10.1103/PhysRevMaterials.6.075006)

## I. INTRODUCTION

ABO<sub>3</sub>-type perovskite oxides have sufficient structural flexibility to generate a wide range of functional properties for electronics and energy storage applications [1–4]. First-row transition metals are the most extensively studied *B*-site elements in these materials. Almost all the transition metals have multiple oxidation states since they readily lose valence electrons to form stable cations [5]. For Ni, the most stable oxidation state is Ni<sup>2+</sup> resulting in NiO being the only stable binary oxide of Ni. Advances in thin-film growth technologies make it possible to synthesize stable rare-earth nickelate RNiO<sub>3</sub> (RNO, where *R* represents a rare-earth lanthanide element) thin films in which Ni is trivalent. Due to the recent discovery of superconductivity in reduced infinite layer R<sub>1-x</sub>Sr<sub>x</sub>NiO<sub>2</sub> thin films [6–11], *A*-site aliovalent substitution of Sr<sup>2+</sup> for R<sup>3+</sup> in the parent RNO perovskite has generated intense scientific interest within the synthesis community. In the absence of oxygen vacancies, Ni assumes a less stable formal charge, 3 + *x*, in R<sub>1-x</sub>Sr<sub>x</sub>NiO<sub>3</sub>. It is thus challenging to synthesize stable, stoichiometric R<sub>1-x</sub>Sr<sub>x</sub>NiO<sub>3</sub> thin films, particularly at high Sr concentration (*x* > 0.3) [12].

In contrast to perovskite RNO, SrNiO<sub>3</sub> (SNO) is expected to form a hexagonal structure as the small ionic radius of Ni<sup>4+</sup> ion leads to a Goldschmidt tolerance factor (*t*) greater

than unity. Previous first-principles density-functional theory (DFT) calculations predict that hexagonal SNO is a ferromagnetic half-metal with promising applications in spintronic devices [13]. Although bulk hexagonal SNO has been synthesized under high pressure (*P*<sub>O<sub>2</sub></sub> > 50 atm) [14], there was a scarcity of data to support the presence of Ni<sup>4+</sup> in this lattice. It was also reported that the cubic perovskite SrFe<sub>1-x</sub>Ni<sub>x</sub>O<sub>3</sub> (0 ≤ *x* ≤ 0.5) can be stabilized under high-pressure and high-temperature conditions although extensive NiO secondary phase formation was observed for *x* > 0.5 [15]. The cubic lattice parameter (~3.81 Å) for bulk SNO was extracted from a linear fit of the lattice parameter dependence on *x* [15]. Our recent efforts to stabilize SNO thin films on perovskite substrates by oxide molecular beam epitaxy (MBE) led to spontaneous phase segregation. As a result, two coexisting, oxygen-deficient Ruddlesden-Popper phases (Sr<sub>2</sub>NiO<sub>3</sub> and SrNi<sub>2</sub>O<sub>3</sub>) were observed [16].

By limiting the SNO layer thickness at the single unit cell (u.c.) level, we have demonstrated that cubic perovskite structured SNO can be stabilized when incorporated into superlattices (SLs) with LaFeO<sub>3</sub> (LFO) [17]. However, strong overlap between the Ni 2*p* and La 3*d* x-ray photoemission core levels precludes obtaining clean Ni 2*p* spectra, and large lattice distortions from LFO layers obscure the intrinsic structural and electronic properties of SNO. Here we replace LFO with SrTiO<sub>3</sub> (STO) to form the SNO/STO SLs [Fig. 1(a)]. The reason for choosing STO is fourfold. First, both Ti 2*p* x-ray photoelectron spectroscopy (XPS) and Ti *L* edge x-ray absorption spectroscopy (XAS) features are well separated from

\*le.wang@pnnl.gov

†yingge.du@pnnl.gov

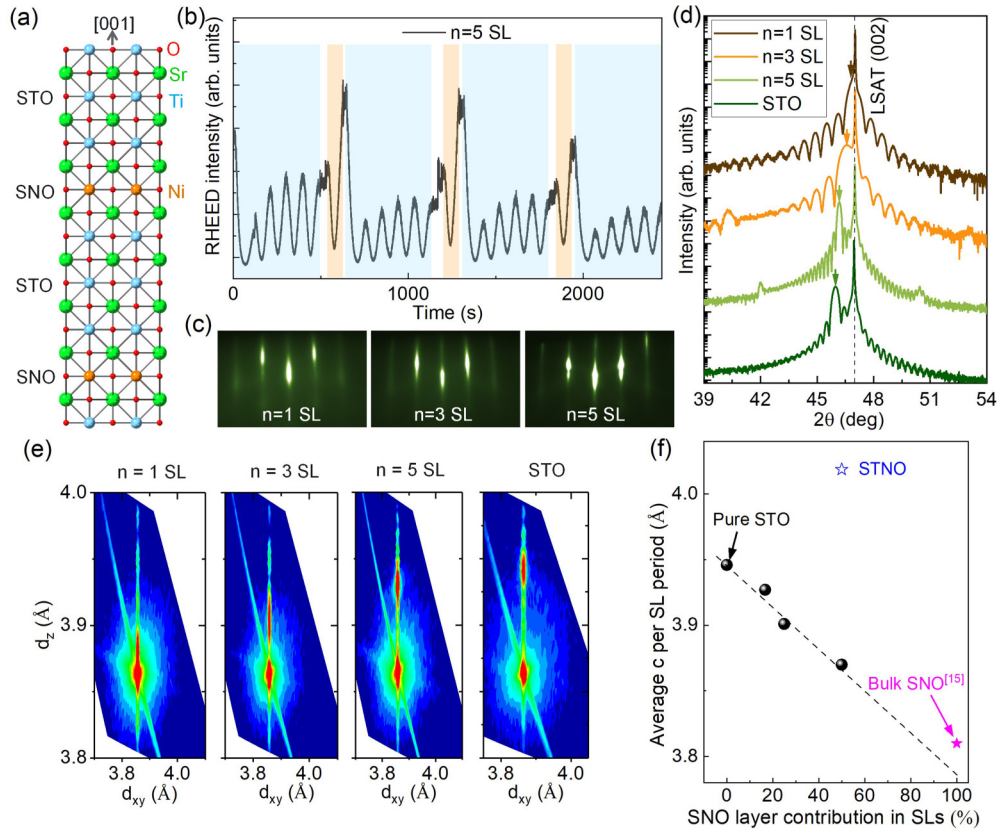


FIG. 1. Synthesis of epitaxial  $(\text{SNO}_1/\text{STO}_n)_k$  SLs and structural characterization. (a) Schematic diagram showing that one unit cell SNO is confined in the SLs with STO. (b) RHEED intensity oscillations of the specular reflected beam during the growth of the  $n = 5$  SL. Blue-shaded areas mark the deposition of STO and yellow-shaded areas mark the deposition of SNO. (c) RHEED patterns for three SLs after growth viewed along the  $[100]$  zone axis. (d) High-resolution XRD  $\theta$ - $2\theta$  scans for these SLs and one pure STO film grown on the same substrate. The  $k$  values are 20, 9, and 20 for  $n = 1, 3,$  and  $5$  SLs, respectively. The LSAT substrate peaks are marked by a dashed line and arrows denote the main SL peaks and the (002) diffraction peak for the STO film. (e) RSM near the 103 reflections for  $n = 1, 3, 5$  SLs and pure STO film, confirming structural coherence. (f) Average out-of-plane lattice constant  $c$  as a function of the SNO layer contribution in SLs.  $c$  values of the STNO solid solution and bulk cubic SNO are also included for comparison.

the analogous Ni spectra. Second, cubic STO ( $a_c = 3.905 \text{ \AA}$ ) without any oxygen octahedral rotations (OORs) and/or  $A$ -site displacements provides a good structural/symmetry match for single-layer SNO. Third, there is no polarity difference between the two (nonpolar) materials, SNO and STO. Finally, tetravalent (formally  $3d^0$ ) Ti is exceedingly stable in STO under all environmental conditions [18]. As a result, charge transfer is not expected to occur at the SNO/STO interface and the intrinsic electronic properties of SNO should be preserved.

We examine the structural and electronic properties of  $\text{SNO}_1/\text{STO}_n$  SLs synthesized by oxide MBE in which the STO layer thickness ( $n$ ) is varied from 1 to 5 u.c. The characterization results are compared with those of pure STO and solid solution  $\text{SrTi}_{0.5}\text{Ni}_{0.5}\text{O}_{3-\delta}$  (STNO) thin films. X-ray diffraction (XRD) and scanning transmission electron microscopy (STEM) measurements confirmed the high crystalline quality of these  $\text{SNO}_1/\text{STO}_n$  SLs. *In situ* XPS and *ex situ* XAS were used to probe the interface electronic structure and valences of the  $B$ -site cations (Ni and Ti). Our results reveal that the Ni valence for  $\text{SNO}_1/\text{STO}_n$  SLs exceeds  $3+$  but is not  $4+$ , whereas the Ti valence is  $4+$ . These formal charges do not change with  $n$ , indicating that there is no charge

transfer across the SNO/STO interface. Valence band offset (VBO) analysis further demonstrates that holes are confined to the SNO layers, consistent with the hole hopping conduction mechanism revealed by in-plane transport measurements. Our findings have significant implications for the controlled engineering of Ni valence in complex nickelates.

## II. RESULTS AND DISCUSSION

A set of  $\text{SNO}_1/\text{STO}_n$  SLs, one 30 nm thick STO film, and one 10 nm thick STNO film, were deposited on (001)-oriented  $(\text{LaAlO}_3)_{0.3}(\text{Sr}_2\text{AlTaO}_6)_{0.7}$  (LSAT) substrates by oxide MBE with assistance of *in situ* reflection high-energy electron diffraction (RHEED) to monitor the growth (see the Experimental Methods section of the Supplemental Material [19]). LSAT with its pseudocubic lattice constant of  $\sim 3.868 \text{ \AA}$  was used as the substrate because of its small in-plane lattice mismatch with STO and SNO. To stabilize the perovskite phase SNO in SLs [17], the SNO layer thickness was set to 1 u.c. while  $n$  varies from 1 to 3 to 5 u.c. The clear RHEED intensity oscillations during the growth [Fig. 1(b)] demonstrate a two-dimensional (2D) layer-by-layer film growth mode. The RHEED patterns of  $\text{SNO}_1/\text{STO}_n$  SLs after growth [Fig. 1(c)]

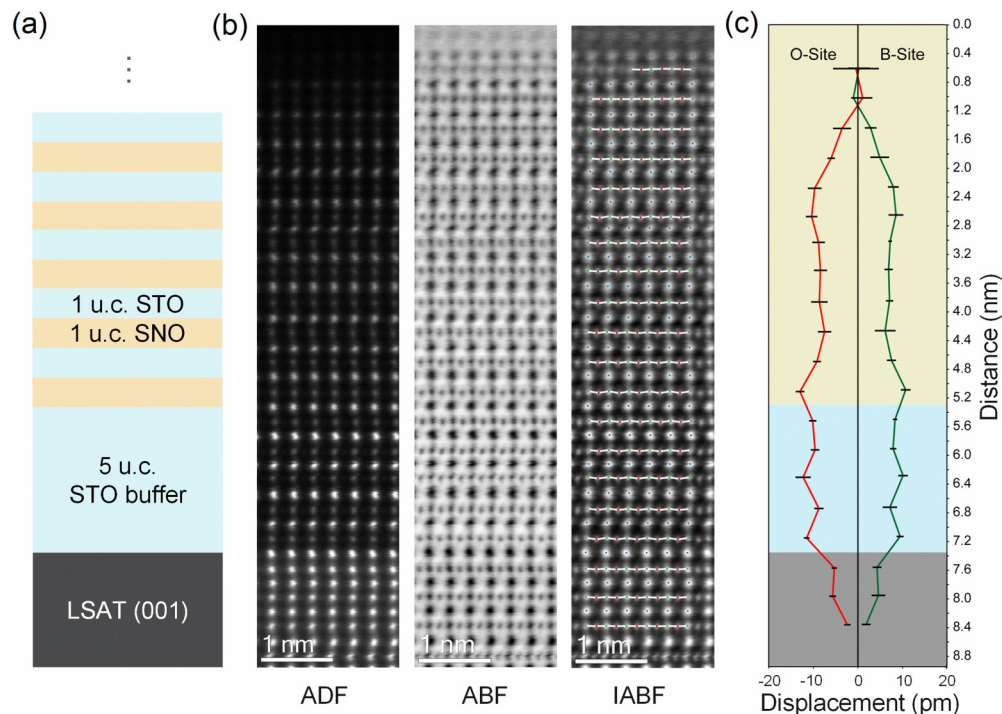


FIG. 2. STEM analysis of interface structure and lattice distortions. (a) Structural diagram for the 5 u.c. STO-buffered  $(\text{SNO}_1/\text{STO}_n)_k$  SL with  $n = 1$ . (b) Cross-sectional template-matched STEM ADF, ABF, and IABF images of the  $n = 1$  SL along the  $[110]$  substrate orientation. Fitted bonds are overlaid on the IABF as white lines. (c) Average fitted  $B$ -site (green) and  $O$  (red) sublattice plane displacements relative to their mean as a function of distance from the surface.

exhibit sharp, bright streaks characteristic of the desired perovskite structure and no additional diffraction spots that would otherwise indicate the presence of secondary phases. In contrast, the RHEED pattern of the STNO solid solution indicates a much rougher surface and a mix of phases (see Fig. S1 of the Supplemental Material [19]). Figure 1(d) shows high-resolution XRD  $\theta$ - $2\theta$  scans in the vicinity of the LSAT(002) peak for the SLs and pure STO film. The presence of clear SL Bragg peaks and SL thickness fringes indicates good crystallinity. Representative x-ray reflectivity (XRR) scans and related modeling (see Fig. S2 of the Supplemental Material [19]) further confirm the overall structural quality of these SLs. All SLs and pure STO film were found to be coherently strained to LSAT according to reciprocal space maps (RSMs) [Fig. 1(e)]. The SL Bragg angle shifts to a higher  $2\theta$  value with decreasing  $n$  in  $\text{SNO}_1/\text{STO}_n$  SLs, indicating that the average out-of-plane lattice constant ( $c$ ) decreases. As shown in Fig. 1(f),  $c$  decreases almost linearly with increasing contribution from the SNO layers in  $\text{SNO}_1/\text{STO}_n$  SLs. A linear fit shows a  $c$  value of  $\sim 3.78$  Å for pure SNO, smaller than that ( $\sim 3.81$  Å) of bulk cubic SNO due to the tensile strain effect imposed by the LSAT substrate, confirming that the cubic perovskite phase SNO was successfully stabilized in these  $\text{SNO}_1/\text{STO}_n$  SLs. On the other hand, the  $c$  value of the STNO solid solution is much larger than that of the  $n = 1$  SL, indicating the likely formation of oxygen vacancies in STNO as a result of the instability of high Ni valence states.

To better understand the local crystal structure and OOR behavior for the  $\text{SNO}_1/\text{STO}_n$  SLs, we performed STEM measurements. A schematic diagram for a  $n = 1$  SL deposited

on a buffer layer of 5 u.c. STO is seen in Fig. 2(a). Figure 2(b) shows the template-matched STEM annular dark field (ADF), annular bright field (ABF), and inverted ABF (IABF) images for a typical  $n = 1$  SL. The expected epitaxial relationship is clearly present, and the interfaces are free of dislocations. However, atomic-scale electron energy loss spectroscopy (EELS) maps of a representative  $n = 5$  SL (see Fig. S3 of the Supplemental Material [19]) reveal some  $B$ -site cation interdiffusion across the SNO/STO interface. Here we measure  $B$ -site and  $O$  sublattice displacements to estimate the degree of OOR, as shown in Fig. 2(c) and Fig. S4 of the Supplemental Material [19] (see Refs. [20–22]). We observe substantial sublattice displacements (8–10 pm) in the 5 u.c. STO buffer, but only 5–6 pm in the first half of the SL and essentially zero at the crystal surface. This overall trend agrees with the expected strain near the buffer and potential relaxation at the sample surface. We note that 2–3 pm displacements are also measured in the LSAT substrate for which the displacements are nominally zero, suggesting that the uncertainty in the SL displacements is  $\pm 3$  pm. Thus, the SL displacements are  $6 \pm 3$  pm, which are nearly negligible [23]. Furthermore, some beam-induced damage is visible in the topmost layers of the crystal which may impact the displacement measurements there. Increasing  $n$  in  $\text{SNO}_1/\text{STO}_n$  SLs causes the structural properties of the STO layers to approach those of bulk STO [Figs. 1(d) and 1(f)]. Thus, the oxygen displacements and associated OORs are negligible in these  $\text{SNO}_1/\text{STO}_n$  SLs, different from the  $\text{SNO}_1/\text{LFO}_n$  SLs in which LFO layers strongly affect the OORs and then tune the  $B$ -site cation valences [17].

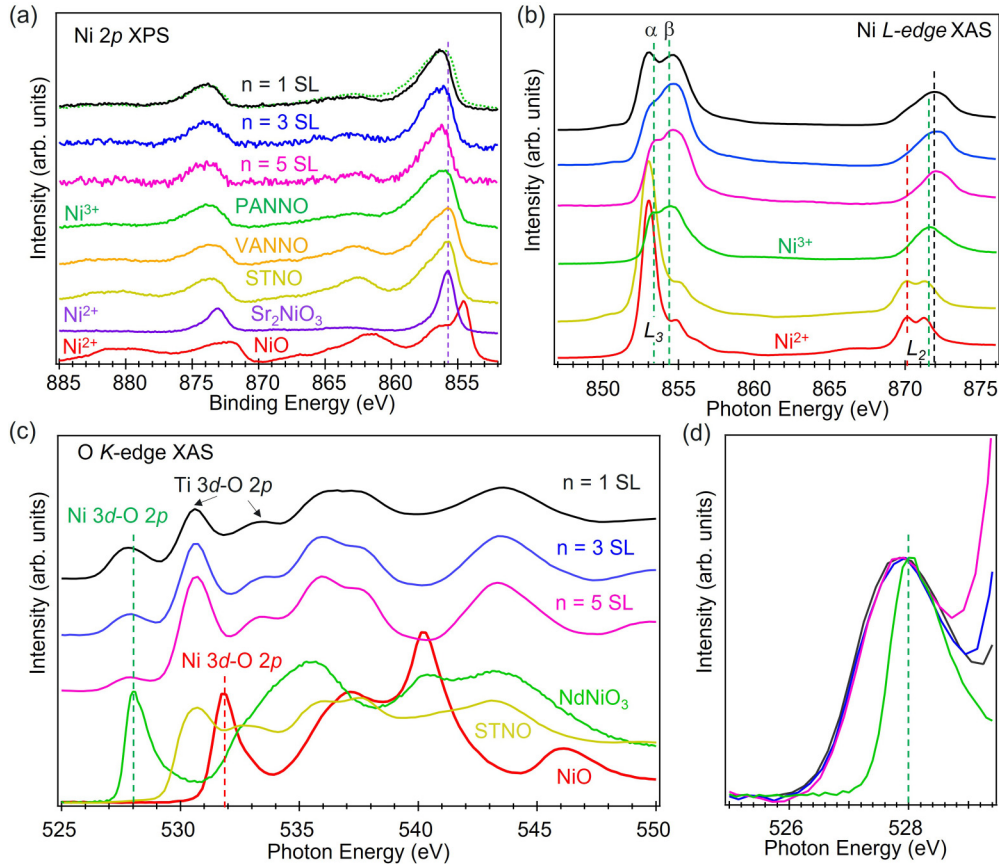


FIG. 3. XPS and XAS results. The spectra of plasma-annealed NdNiO<sub>3</sub> (PANNO), vacuum-annealed NdNiO<sub>3- $\delta$</sub>  (VANNO), Sr<sub>2</sub>NiO<sub>3</sub>, and NiO taken from Ref. [16] are included for reference. (a) *In situ* Ni 2*p* XPS. The dashed purple line denotes the 2*p*<sub>3/2</sub> binding energy for Sr<sub>2</sub>NiO<sub>3</sub>. For comparison, we overlay the Ni 2*p* spectrum of the PANNO (dotted green) on that of the *n* = 1 SL. (b) Ni *L*-edge XAS. The dashed red, green, and black lines denote the photon energies for Ni<sup>2+</sup>, Ni<sup>3+</sup> references, and the *n* = 1 SL, respectively. (c) O *K*-edge XAS. The dashed red and green lines denote the hybridization of the O 2*p* states with Ni 3*d* states. (d) Normalized prepeak features in O *K*-edge XAS.

To study the effect of *n* on the *B*-site cation valences in SNO<sub>1</sub>/STO<sub>*n*</sub> SLs, *in situ* XPS and *ex situ* XAS measurements were performed. A plasma-annealed NdNiO<sub>3</sub> film (PANNO) was used as a Ni<sup>3+</sup> standard and a vacuum-annealed NdNiO<sub>3- $\delta$</sub>  film (VANNO), a Sr<sub>2</sub>NiO<sub>3</sub> film, and a NiO film were used as Ni<sup>2+</sup> standards [16]. It is well known that Ni 2*p* XPS and *L*-edge XAS line shapes in transition metal (TM)-containing oxides can exhibit multiplet fine structure due to angular momentum coupling of the unpaired 3*d* valence electrons to the unpaired 2*p* core electron following 2*p* photoionization [24,25]. Additionally, in the case of XPS, valence charge arrangement in response to the strong electronic perturbation generated by core-hole creation (“shake” phenomena) leading to prominent charge-transfer (CT) satellite peaks not seen in spectra for the pure TM element is quite common in oxides containing TM cations [26]. CT satellites are generally weak in XAS due to screening of the core hole by the excitonic final state [27]. The different local atomic and electronic structures found in different crystal lattices can result in very different Ni 2*p* XPS and *L*-edge XAS.

Figure 3(a) shows Ni 2*p* XPS spectra for the three SLs, STNO, and the four reference samples mentioned above. All spectra were shifted so the corresponding O 1*s* peaks fall at

530.0 eV. The spectra for SNO<sub>1</sub>/STO<sub>*n*</sub> SLs are very similar, and their line shapes closely resemble that of PANNO. The Ni 2*p*<sub>3/2</sub> features for SNO<sub>1</sub>/STO<sub>*n*</sub> SLs are shifted to slightly higher binding energy (~0.2 eV) relative to that of PANNO. This result suggests that the Ni valence in the SNO<sub>1</sub>/STO<sub>*n*</sub> SLs may slightly exceed 3+. However, the Ni valence is clearly not 4+ as the chemical shift in both XPS and XAS peak centroids is roughly +1 eV per unit increase in valence for most of the 3*d* transition metal (TM) oxides [28–33]. In contrast, the Ni 2*p* spectrum for STNO is very similar to that for VANNO, and the Ni 2*p*<sub>3/2</sub> feature peak energy is the same as that of VANNO and Sr<sub>2</sub>NiO<sub>3</sub>, indicating that the Ni valence in STNO is Ni<sup>2+</sup>. It is noteworthy that the primary *j* = 3/2 and 1/2 spin-orbit components in the Ni 2*p* spectrum for rocksalt NiO fall at significantly lower binding energies than those for the perovskites Sr<sub>2</sub>NiO<sub>3</sub> and VANNO despite the three materials containing Ni with nominally the same valence. This result indicates that the practice of calibrating the Ni 2*p* spectra using a constant O 1*s* binding energy of 530.0 eV may not be reliable when going from one lattice structure to another.

The Ni valence assignment from Ni 2*p* XPS is corroborated by XAS measurements at the Ni *L* edge. As shown in Fig. 3(b), we compare the Ni *L*-edge XAS for SNO<sub>1</sub>/STO<sub>*n*</sub>

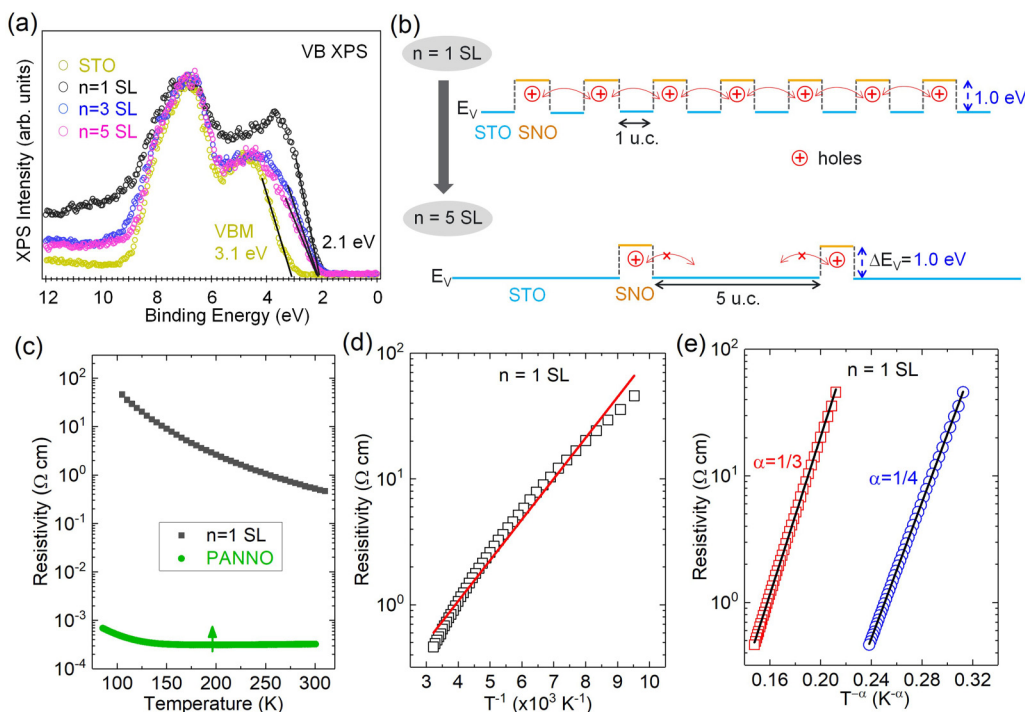


FIG. 4. Valence band offset (VBO,  $\Delta E_v$ ) analysis and in-plane transport results. (a) VB spectra for pure STO film and SNO<sub>1</sub>/STO<sub>n</sub> SLs with  $n$  ranging from 1 to 5. Ti 2*p* spectra were used to align these VB spectra. VBMs are obtained by linear extrapolation of the leading edge to the energy axis. (b) Energy band-edge diagram for the STO<sub>1</sub>/SNO<sub>n</sub> SLs resulting from band alignment analysis. (c) Resistivity ( $\rho$ ) vs temperature curves on warming for the  $n = 1$  SL and PANNO. (d) Resistivity as a function of  $1/T$  over the range of 100–310 K. (e) Resistivity as a function of  $T^{-\alpha}$  over the range of 100–310 K.

SLs and STNO with those of reference samples of PANNO (Ni<sup>3+</sup> valence state) and NiO (Ni<sup>2+</sup> valence state). For PANNO, there are two distinct peaks at the Ni *L*<sub>3</sub> edge (labeled  $\alpha$  and  $\beta$ ), located at 853.3 and 854.3 eV, respectively, and a single feature located at  $\sim$ 871.6 eV at the Ni *L*<sub>2</sub> edge. The NiO spectrum shows a two-peak structure at both the *L*<sub>3</sub> and *L*<sub>2</sub> edges and the spectral feature at the *L*<sub>3</sub> edge shows a sharp increase (decrease) in the intensity of peak  $\alpha$  ( $\beta$ ) as well as a shift to lower (higher) photon energy relative to PANNO. The Ni *L* edges for the SNO<sub>1</sub>/STO<sub>n</sub> SLs are similar to that of PANNO except for feature  $\beta$ . Both *L*<sub>2</sub> edges and corresponding  $\beta$  features at *L*<sub>3</sub> edges slightly shift toward higher photon energy compared to the Ni<sup>3+</sup> reference (PANNO). This indicates that the Ni valence for SNO<sub>1</sub>/STO<sub>n</sub> SLs exceeds 3+, which is consistent with our XPS results shown in Fig. 3(a). We note that the spectral weight of feature  $\alpha$  at the Ni *L*<sub>3</sub> edge for the  $n = 1$  SL is comparable to that of feature  $\beta$ , suggesting that the average Ni valence for the  $n = 1$  SL is lower than that for the  $n = 3$  and 5 SLs [32,34,35]. The lower Ni valence for the  $n = 1$  SL is likely associated with some degree of Ni/Ti intermixing and/or air exposure and degradation before XAS measurements. We also compare the Ni *L*-edge XAS for the  $n = 1$  SL and the STNO solid solution. The Ni spectrum of the STNO solid solution is very similar to that of NiO, indicating that the Ni valence state in STNO is Ni<sup>2+</sup>, consistent with the larger  $c$  value deduced from XRD [Fig. 1(f)], and highlighting the differences between the SL and the solid solution with the same volume-averaged composition. Figure S5 of the Supplemental Material [19] displays the normalized Ti *L*-edge XAS of SNO<sub>1</sub>/STO<sub>n</sub> SLs. No changes in peak shape and peak

position are observed when changing  $n$ . The Ti *L*-edge XAS are in good agreement with that previously reported for pure STO [36], confirming that the Ti valence in SNO<sub>1</sub>/STO<sub>n</sub> SLs is Ti<sup>4+</sup>. Thus, all the above spectroscopic data confirm that there is no charge transfer across the STO/SNO interface.

For 3*d* TM oxides, increasing the valence of the TM cation lowers the absorption energy of its 3*d* unoccupied states. When the TM cation is bound to oxygens, it undergoes TM 3*d*–O 2*p* hybridization, resulting in a lower x-ray absorption energy for the O *K* pre-edge peak. For example, a higher TM oxidation state gives rise to a lower O *K* pre-edge peak energy [37]. Thus, the pre-edge spectral feature at the O *K* edge is very sensitive to changes in the TM oxidation state. In this fashion, we measured the O *K* pre-edge features for these SNO<sub>1</sub>/STO<sub>n</sub> SLs to further analyze the Ni valence. As shown in Figs. 3(c) and 3(d), the O *K* pre-edge peaks for SNO<sub>1</sub>/STO<sub>n</sub> SLs are located at the same photon energy (about 527.8 eV), which is slightly lower than the pre-edge peak for PANNO (about 528 eV). This pre-edge feature is consistent with a Ni oxidation state slightly higher than 3+ in the SLs [37]. Moreover, the O *K* pre-edge peak width for SNO<sub>1</sub>/STO<sub>n</sub> SLs is greater than that for PANNO [Fig. 3(d)], suggesting a stronger Ni 3*d*–O 2*p* hybridization for SNO layers in SNO<sub>1</sub>/STO<sub>n</sub> SLs [38], further supporting that the Ni valence for SNO<sub>1</sub>/STO<sub>n</sub> SLs is higher than 3+.

Figure 4(a) shows the valence band (VB) spectra for three SNO<sub>1</sub>/STO<sub>n</sub> ( $n = 1, 3, 5$ ) SLs along with that of pure STO film. All spectra were shifted such that the corresponding Ti 2*p*<sub>3/2</sub> peaks fall at the same binding energy as that for pure STO film. Three SLs show the same VB maximum (VBM)

value ( $\sim 2.1$  eV), which is smaller than that of pure STO film by  $\sim 1$  eV. Determining accurate VB offsets (VBOs) from XPS as described by Kraut *et al.* [39] is precluded by the fact that a reference specimen of thick-film perovskite SNO could not be synthesized due to its instability [16]. Here we utilize an approximate method instead. Based on the observation that the VBM values of the SLs are lower in binding energy than that of pure STO film, we intuit that the top portions of the SL VBs are SNO derived [17]. As a result, the VBO can be estimated as  $\Delta E_{V\approx E_V(\text{STO})-E_V(\text{SL})}$ . The same VBM value for different  $n$  in  $\text{SNO}_1/\text{STO}_n$  SLs leads to the same  $\Delta E_V$  value ( $\sim 1.0$  eV). Thus, holes are confined to the SNO layers in  $\text{SNO}_1/\text{STO}_n$  SLs [Fig. 4(b)]. Figure 4(c) shows resistivity vs temperature ( $\rho$ - $T$ ) curves for the  $n = 1$  SL and the reference Panno film. The  $n = 3$  and 5 SLs are too resistive to measure with our current experimental setup. The reference Panno film shows metallic bulklike  $\rho$ - $T$  behavior with low resistivity of  $\sim 3.2 \times 10^{-4} \Omega \text{ cm}$  at 300 K, while the  $n = 1$  SL exhibits semiconducting behavior with high resistivity of  $0.52 \Omega \text{ cm}$  at 300 K.

To gain further insight into the conduction mechanism for these SLs, the transport behavior of the  $n = 1$  SL was fitted to two different models as shown in Figs. 4(d) and 4(e). Attempts to fit the  $\rho$ - $T$  curve for the  $n = 1$  SL to a simple activated model [ $\rho = \rho_0 \exp(E_A/k_B T)$ ] failed, as there is a clear curvature in the Arrhenius plot [Fig. 4(d)]. We note that variable range hopping (VRH) type of conduction has been observed in both ultrathin RNO films and several RNO-based SLs [40–42]. Thus, the VRH model [ $\rho = \rho_0 \exp(T_0/T)^\alpha$ ] was also used to fit the  $\rho$ - $T$  curve of the  $n = 1$  SL. As seen in Fig. 4(e), both two-dimensional 2D ( $\alpha = 1/3$ ) and 3D ( $\alpha = 1/4$ ) VRH models fit well, suggesting that conduction in  $\text{SNO}_1/\text{STO}_n$  SLs is due to holes hopping in SNO layers. The  $\text{SNO}_1/\text{STO}_n$  SL can be considered as a periodic set of multiple quantum wells in which  $n$  u.c. STO layers separate the individual wells [see schematic in Fig. 4(b)]. For the  $n = 1$  SL, since carriers (holes here) can tunnel through the barriers between quantum wells and the wave functions of neighboring wells couple together, the electronic states form delocalized minibands and semiconducting behavior is observed. With increasing  $n$  from 1 to 3 and 5, barriers between quantum wells are sufficiently wide such that carriers cannot tunnel through, which strongly suppresses hole hopping along the  $c$ -axis direction [43] and makes the system more localized and insulating.

We also measured the magnetic properties of these SLs. No obvious magnetic moment is observed over the temperature range 5–300 K (not shown here), whereas recent DFT simulations indicate ferromagnetic coupling between the Ni cations in the cubic perovskite  $\text{SrNiO}_{3-\delta}$  and that the removal of oxygen (i.e., larger  $\delta$ ) increases the net magnetization [44]. Insertion of STO layers between ultrathin SNO layers in our SNO/STO SLs breaks the long-range ferromagnetic coupling that exists in pure SNO, presumably resulting in the absence of ferromagnetism we have observed.

### III. CONCLUSIONS AND PROSPECTS

In summary, we have synthesized a series of  $\text{SNO}_1/\text{STO}_n$  SLs grown on (001)-oriented LSAT substrates by oxide MBE and investigated the effect of  $n$  on lattice structure, electronic properties, and transport behavior. We found that  $\text{SNO}_1/\text{STO}_n$  SLs exhibit high structural quality and are coherently strained to LSAT substrates. The Ti valence is 4+ while the Ni valence exceeds 3+ but is not 4+, and neither valence changes with  $n$ . In contrast, the STNO solid solution exhibits low structural quality and lots of oxygen vacancies, driving the Ni valence down to 2+. In-plane transport data are consistent with variable-range hole hopping conductivity for the  $n = 1$  SL. However, hole hopping along the  $c$ -axis direction was strongly suppressed when increasing  $n$  to 3 and 5, resulting in insulating behavior. Our work further highlights that the structural environment of complex materials can be controlled to achieve electronic structures that are not found in analogous bulk materials by means of SL formation. It is thus of interest to use the same approach to synthesize the  $\text{SNO}_1/\text{RNO}_n$  SLs and compare the resulting electronic properties and transport data to that of solid solutions with the same volume-averaged composition, i.e.,  $\text{R}_{1-x}\text{Sr}_x\text{NiO}_3$  where  $x = 1/(n + 1)$ . Doing so may open avenues for studying superconductivity in nickel-based oxides. Ongoing studies in our lab are investigating the impact of strain and lattice orientation on the structure and properties of  $\text{SrNiO}_3$  films and heterostructures. Further experimental investigations will address how to suppress the formation of oxygen vacancies during the growth and/or cooling process for  $\text{SrNiO}_3$  films.

Supporting information is available online or from the author.

### ACKNOWLEDGMENTS

This work was supported by the U.S. Department of Energy (DOE), Office of Science, Office of Basic Energy Sciences, Division of Materials Sciences and Engineering under Award No. 10122. We acknowledge facility support from W. R. Wiley Environmental Molecular Sciences Laboratory, a DOE User Facility sponsored by the Office of Biological and Environmental Research. We thank Dr. Peter V. Sushko for valuable discussions. The soft x-ray absorption spectroscopy experiments were carried out at the SSRL (beamline 13-3), SLAC National Accelerator Laboratory, supported by the U.S. Department of Energy, Office of Science, Office of Basic Energy Sciences under Contract No. DE-AC02-76SF00515. Part of this work was carried out with the support of the 4B9B beamline at Beijing Synchrotron Radiation Facility. A portion of the microscopy work was performed in the Radiological Microscopy Suite (RMS), located in the Radiochemical Processing Laboratory (RPL) at PNNL.

The authors declare no competing financial interests.

[1] N. Reyren, S. Thiel, A. D. Caviglia, L. Fitting Kourkoutis, G. Hammerl, C. Richter, C. W. Schneider, T. Kopp, A.-S. Ruetschi, D. Jaccard, M. Gabay, D. A. Muller, J.-M. Triscone, and J. Mannhart, *Science* **317**, 1196 (2007).

[2] I. Grinberg, D. Vincent West, M. Torres, G. Gou, D. M. Stein, L. Wu, G. Chen, E. M. Gallo, A. R. Akbashev, P. K. Davies, J. E. Spanier, and A. M. Rappe, *Nature (London)* **503**, 509 (2013).

- [3] Y. Zhou, X. Guan, H. Zhou, K. Ramadoss, S. Adam, H. Liu, S. Lee, J. Shi, M. Tsuchiya, D. D. Fong, and S. Ramanathan, *Nature (London)* **534**, 231 (2016).
- [4] J. Hwang, R. R. Rao, L. Giordano, Y. Katayama, Y. Yu, and Y. Shao-Horn, *Science* **358**, 751 (2017).
- [5] H. Raebiger, S. Lany, and A. Zunger, *Nature (London)* **453**, 763 (2008).
- [6] D. Li, K. Lee, B. Y. Wang, M. Osada, S. Crossley, H. R. Lee, Y. Cui, Y. Hikita, and H. Y. Hwang, *Nature (London)* **572**, 624 (2019).
- [7] Q. Gu, Y. Li, S. Wan, H. Li, W. Guo, H. Yang, Q. Li, X. Zhu, X. Pan, Y. Nie, and H. H. Wen, *Nat. Commun.* **11**, 6027 (2020).
- [8] D. Li, B. Y. Wang, K. Lee, S. P. Harvey, M. Osada, B. H. Goodge, L. F. Kourkoutis, and H. Y. Hwang, *Phys. Rev. Lett.* **125**, 027001 (2020).
- [9] M. Osada, B. Y. Wang, B. H. Goodge, K. Lee, H. Yoon, K. Sakuma, D. Li, M. Miura, L. F. Kourkoutis, and H. Y. Hwang, *Nano Lett.* **20**, 5735 (2020).
- [10] S. Zeng, C. S. Tang, X. Yin, C. Li, M. Li, Z. Huang, J. Hu, W. Liu, G. J. Omar, H. Jani, Z. S. Lim, K. Han, D. Wan, P. Yang, S. J. Pennycook, A. T. S. Wee, and A. Ariando, *Phys. Rev. Lett.* **125**, 147003 (2020).
- [11] M. Osada, B. Y. Wang, B. H. Goodge, S. P. Harvey, K. Lee, D. Li, L. F. Kourkoutis, and H. Y. Hwang, *Adv. Mater.* **33**, 2104083 (2021).
- [12] K. Lee, B. H. Goodge, D. Li, M. Osada, B. Y. Wang, Y. Cui, L. F. Kourkoutis, and H. Y. Hwang, *APL Mater.* **8**, 041107 (2020).
- [13] G. Y. Chen, C. L. Ma, D. Chen, and Y. Zhu, *J. Solid State Chem.* **233**, 438 (2016).
- [14] Y. Takeda, T. Hashino, H. Miyamoto, F. Kanamaru, S. Kume, and M. Koizumi, *J. Inorg. Nucl. Chem.* **34**, 1599 (1972).
- [15] H. Seki, T. Saito, and Y. Shimakawa, *J. Jpn. Soc. Powder Powder Metall.* **63**, 609 (2016).
- [16] L. Wang, Z. Yang, X. Yin, S. D. Taylor, X. He, C. S. Tang, M. E. Bowden, J. Zhao, J. Wang, J. Liu, D. E. Perea, L. Wangoh, A. T. S. Wee, H. Zhou, S. A. Chambers, and Y. Du, *Sci. Adv.* **7**, eabe2866 (2021).
- [17] L. Wang, Z. Yang, M. E. Bowden, J. W. Freeland, P. V. Sushko, S. R. Spurgeon, B. Matthews, W. S. Samarakoon, H. Zhou, Z. Feng, M. H. Engelhard, Y. Du, and S. A. Chambers, *Adv. Mater.* **32**, 2005003 (2020).
- [18] S. Cook, T. K. Andersen, H. Hong, R. A. Rosenberg, L. D. Marks, and D. D. Fong, *APL Mater.* **5**, 126101 (2017).
- [19] See Supplemental Material at <http://link.aps.org/supplemental/10.1103/PhysRevMaterials.6.075006> for details on experimental methods, code availability, high-resolution XRD  $\theta$ - $2\theta$  scans for the  $n = 1$  SL and the STNO solid solution, x-ray reflectivity, HAADF STEM image and corresponding individual EELS maps, illustration of temwizard processing, and the Ti L edge, which includes Refs. [20–22].
- [20] L. Jones, H. Yang, T. J. Pennycook, M. S. J. Marshall, S. Van Aert, N. D. Browning, M. R. Castell, and P. D. Nellist, *Adv. Struct. Chem. Imaging* **1**, 8 (2015).
- [21] M. Nord, P. E. Vullum, I. MacLaren, T. Tybell, and R. Holmestad, *Adv. Struct. Chem. Imaging* **3**, 9 (2017).
- [22] M. Grinberg, *Flask Web Development: Developing Web Applications with Python* (O'Reilly Media, Inc., Sebastopol, CA, 2018).
- [23] K. Song, T. Min, J. Seo, S. Ryu, H. Lee, Z. Wang, S.-Y. Choi, J. Lee, C.-B. Eom, and S. H. Oh, *Adv. Sci.* **8**, 2002073 (2021).
- [24] G. van der Laan, J. Zaanen, G. A. Sawatzky, R. Karnatak, and J.-M. Esteve, *Phys. Rev. B* **33**, 4253 (1986).
- [25] P. S. Bagus, M. J. Sassi, and K. M. Rosso, *J. Electron Spectrosc. Relat. Phenom.* **200**, 174 (2015).
- [26] P. S. Bagus, E. S. Ilton, and C. J. Nelin, *Surf. Sci. Rep.* **68**, 273 (2013).
- [27] F. M. F. de Groot, H. Elnaggar, F. Frati, R.-P. Wang, M. U. Delgado-Jaime, M. V. Veenendaal, J. Fernandez-Rodriguez, M. W. Haverkort, R. J. Green, and G. van der Laan, *J. Electron Spectrosc. Relat. Phenom.* **249**, 147061 (2021).
- [28] L. Qiao, H. Y. Xiao, S. M. Heald, M. E. Bowden, T. Varga, G. J. Exarhos, M. D. Biegalski, I. N. Ivanov, W. J. Weber, T. C. Droubay, and S. A. Chambers, *J. Mater. Chem. C* **1**, 4527 (2013).
- [29] R. Qiao, L. A. Wray, J.-H. Kim, N. P. W. Pieczonka, S. J. Harris, and W. Yang, *J. Phys. Chem. C* **119**, 27228 (2015).
- [30] N. Lu, P. Zhang, Q. Zhang, R. Qiao, Q. He, H.-B. Li, Y. Wang, J. Guo, D. Zhang, Z. Duan, Z. Li, M. Wang, S. Yang, M. Yan, E. Arenholz, S. Zhou, W. Yang, L. Gu, C.-W. Nan, J. Wu *et al.*, *Nature (London)* **546**, 124 (2017).
- [31] S. Nemrava, D. A. Vinnik, Z. Hu, M. Valldor, C.-Y. Kuo, D. A. Zherebtsov, S. A. Gudkova, C.-T. Chen, L. H. Tjeng, and R. Niewa, *Inorg. Chem.* **56**, 3861 (2017).
- [32] M. Kotiuga, Z. Zhang, J. Li, F. Rodolakis, H. Zhou, R. Sutarto, F. He, Q. Wang, Y. Sun, Y. Wang, N. A. Aghamiri, S. B. Hancock, L. P. Rokhinson, D. P. Landau, Y. Abate, J. W. Freeland, R. Comin, S. Ramanathan, and K. M. Rabe, *Proc. Natl. Acad. Sci. U. S. A.* **116**, 21992 (2019).
- [33] L. Wang, Y. Du, P. V. Sushko, M. E. Bowden, K. A. Stoerzinger, S. M. Heald, M. D. Scafetta, T. C. Kaspar, and S. A. Chambers, *Phys. Rev. Materials* **3**, 025401 (2019).
- [34] J. W. Freeland, M. V. Veenendaal, and J. Chakhalian, *J. Electron Spectrosc. Relat. Phenom.* **208**, 56 (2016).
- [35] L. Wang, L. Chang, X. Yin, L. You, J.-L. Zhao, H. Guo, K. Jin, K. Ibrahim, J. Wang, A. Rusydi, and J. Wang, *Appl. Phys. Lett.* **110**, 043504 (2017).
- [36] J.-S. Lee, Y. W. Xie, H. K. Sato, C. Bell, Y. Hikita, H. Y. Hwang, and C.-C. Kao, *Nat. Mater.* **12**, 703 (2013).
- [37] S. Roychoudhury, R. Qiao, Z. Zhuo, Q. Li, Y. Lyu, J.-H. Kim, J. Liu, E. Lee, B. J. Polzin, J. Guo, S. Yan, Y. Hu, H. Li, D. Prendergast, and W. Yang, *Energy Environ. Mater.* **4**, 246 (2021).
- [38] J. Chakhalian, J. M. Rondinelli, J. Liu, B. A. Gray, M. Kareev, E. J. Moon, N. Prasai, J. L. Cohn, M. Varela, I.-C. Tung, M. J. Bedzyk, S. G. Altendorf, F. Strigari, B. Dabrowski, L. H. Tjeng, P. J. Ryan, and J. W. Freeland, *Phys. Rev. Lett.* **107**, 116805 (2011).
- [39] E. A. Kraut, R. W. Grant, J. R. Waldrop, and S. P. Kowalczyk, *Phys. Rev. Lett.* **44**, 1620 (1980).
- [40] S. J. May, T. S. Santos, and A. Bhattacharya, *Phys. Rev. B* **79**, 115127 (2009).
- [41] R. Scherwitzl, S. Gariglio, M. Gabay, P. Zubko, M. Gibert, and J.-M. Triscone, *Phys. Rev. Lett.* **106**, 246403 (2011).
- [42] H. Wei, M. Jenderka, M. Bonholzer, M. Grundmann, and M. Lorenz, *Appl. Phys. Lett.* **106**, 042103 (2015).
- [43] J. Chaloupka and G. Khaliullin, *Phys. Rev. Lett.* **100**, 016404 (2008).
- [44] E. Cho, K. Klyukin, S. Ning, J. Li, R. Comin, R. J. Green, B. Yildiz, and C. A. Ross, *Phys. Rev. Materials* **5**, 094413 (2021).